High-order exceptional points of counterpropagating waves in weakly deformed microdisk cavities

Julius Kullig* and Jan Wiersig†
Institut für Physik, Otto-von-Guericke-Universität Magdeburg, Postfach 4120, D-39016 Magdeburg, Germany

(Received 1 July 2019; published 25 October 2019)

In a recent publication [Phys. Rev. A **98**, 023851 (2018)] the authors reported on a systematic approach based on perturbation theory to generate non-Hermitian degeneracies, so-called exceptional points, in weakly deformed microdisk cavities by coupling modes of different angular momentum. In the present paper we extent this approach to fully asymmetric boundary deformations. This allows us to increase the order of the exceptional point and create modes with interesting angular momentum patterns where a nonuniform clockwise and counterclockwise propagation is present. Furthermore, we combine the perturbation theory of weakly deformed microdisks with the coupled-mode theory to explain possible measurements of transmission and reflection spectra via a waveguide attached to the cavity.

DOI: 10.1103/PhysRevA.100.043837

I. INTRODUCTION

Open quantum and wave systems exhibit interesting and unconventional effects associated with non-Hermitian physics. One among those phenomena which in the last years attracted enormous scientific attention is exceptional points (EPs) [1–3]. These are points in parameter space at which two or more complex eigenvalues (frequencies) of a non-Hermitian Hamiltonian and simultaneously also the corresponding eigenstates (modes) coalesce. Exceptional points have been observed and experimentally realized in a variety of systems such as microwave cavities [4,5], optical microcavities [6–8], acoustic cavities [9], optical lattices [10], coupled atom-cavity systems [11], nonuniformly pumped lasers [12], and exciton-polariton billiards [13]. Especially, optical whispering-gallery cavities are of great interest to study non-Hermitian physics and EPs [14]. In such cavities clockwise (CW) and counterclockwise (CCW) propagating waves are trapped for very long times. Due to boundary deformations or external perturbations, a scattering between both propagation directions is present. If these systems do not possess a mirror reflection symmetry, e.g., because of an asymmetric boundary deformation, the scattering process from one propagation direction is in general more pronounced than that in the reversed process. As a consequence of this asymmetric backscattering the optical modes are not standing waves but (partially) copropagating traveling waves [15,16]. In its most extreme case at an EP the backscattering in only one direction, e.g., from CW to CCW, is present and the mode itself becomes a purely CCW propagating wave [17,18].

On the other hand, it has been shown recently [19] that EPs can also occur in the spectrum of extremely weak deformed microdisks with symmetric backscattering. Here, an adjustment of the refractive index and a very weak symmetric boundary deformation is sufficient to coalesce modes with different angular momentums. The formation of these EPs is very well described by perturbation theory [20].

The frequencies around an EP of second order (EP2) have the characteristic topology of a complex square root. Hence, slight parameter variations around the EP2 can be amplified to a large response in the (complex) frequency splitting. For applications this mechanism thus qualifies sensors based on EPs to be very sensitive [21–23]. In recent years EPs of higher order where more than two modes coalesce have been considered [24–30]. Here, also the frequency splittings behave like a root of higher order in parameter space, which leads to a further improvement of the sensor's sensitivity [30].

In this paper we combine the two approaches, asymmetric backscattering and quasidegenerate mode pairs, to generate such an EP of high order. More precisely, we show that a small but fully asymmetric boundary deformation is capable to achieve an EP of fourth order (EP4) where four modes coalesce. Moreover, we combine the derived perturbative description of the deformed cavity with coupled-mode theory. This allows us to explain typical experimental situations where the transmission and reflection spectra of a deformed cavity is measured via an attached waveguide.

The paper is organized as follows. In Sec. II we give a review of the quasi-two-dimensional microdisk cavity. The extension of the perturbation theory to quasidegenerate modes in a fully asymmetric deformed microdisk is discussed in Sec. III. Two example deformations for an EP4 are presented in Sec. IV. In Sec. V the cross section for plane-wave scattering is shown, and in Sec. VI transmission and reflection coefficient measurements via an attached waveguide are discussed. A summary is given in Sec. VII.

II. REVIEW ON MODES IN A CIRCULAR CAVITY

Optical microdisk cavities are well described within a quasi-two-dimensional approximation. Here, Maxwell's equations reduce to a scalar mode equation [31],

$$[\Delta + n^2 k^2]\psi = 0, \tag{1}$$

*julius.kullig@ovgu.de
†jan.wiersig@ovgu.de

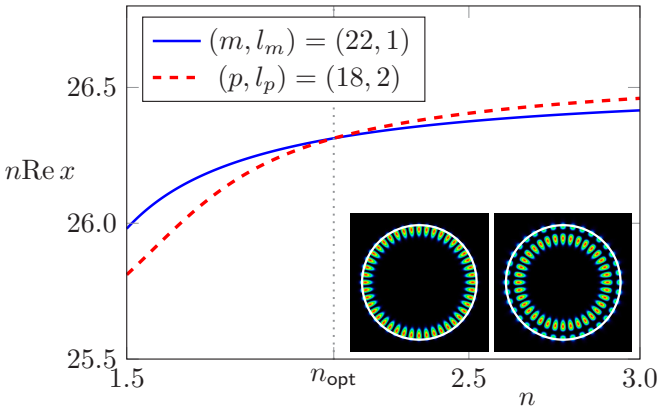

FIG. 1. Scaled real part of the dimensionless complex frequency of mode (solid blue curve) $(m, l_m) = (22, 1)$ and (dashed red curve) $(p, l_p) = (18, 2)$. The insets show the corresponding intensity patterns $|\psi|^2$ in a circular cavity with $n_{\mathrm{opt}} = 2.105\,094\,8$.

where $\mathrm{Re}\,(\psi e^{-i\omega t})$ represents the z component of the electric or magnetic field for transverse magnetic (TM) or transverse electric (TE) polarization, and ω is the complex frequency. The finite height of the cavity is taken into account by n being the effective refractive index. At the cavity's interface the wave function ψ and its scaled normal derivative $\zeta^{-2}\partial_\nu\psi$ are continuous with $\zeta = 1$ (n) for TM (TE) polarization. The modes are described by the (dimensionless) complex frequency $x \equiv kR = \omega R/c$; R is the radius of the microdisk and c is the speed of light in vacuum. The quality factor is thus given by $Q = -\mathrm{Re}\, x/(2\mathrm{Im}\, x)$.

In case of a circular cavity the rotational symmetry can be exploited to determine the frequencies of the modes (for TM polarization) as roots of

$$S_m(x) = n\frac{J_m'}{J_m}(nx) - \frac{H_m'}{H_m}(x). \tag{2}$$

Here, J_m and H_m are Bessel and Hankel functions of the first kind and order m. The derivative with respect to the argument is denoted by a prime ($'$). Note that the roots of S_m are doubly degenerate for $m \neq 0$, reflecting the equivalence of CW and CCW propagation in the circular cavity.

The wave function ψ is given in polar coordinates by

$$\psi_m(r, \phi; x) = \chi_m(\phi)\begin{cases} \frac{J_m(nkr)}{J_m(nx)} & r \leqslant R \\ \frac{H_m(kr)}{H_m(x)} & r > R \end{cases}. \tag{3}$$

For the angular dependency $\chi_m(\phi)$ it is convenient to distinct two sets of basis functions: the traveling-wave basis with $\chi_m(\phi) = e^{im\phi}$ with $m = 0, \pm1, \pm2, \pm3, \ldots$ and the standing wave basis with $\chi_m(\phi) \in \{\cos(m\phi), \sin(m\phi)\}$ with $m = 0, 1, 2, 3, \ldots$. In both cases m is called the azimuthal mode number.

The solutions of $S_m(x) = 0$ for fixed m corresponding to well-confined whispering-gallery modes can be labeled with the radial mode number l_m reflecting the number of the wave function's local maxima in radial direction. Note that besides these modes with large Q factors there exist also modes with very short lifetimes, called external modes [32–35], which will be omitted here.

The complex frequencies x depend on the refractive index n. This is shown for the modes $(m, l_m) = (22, 1)$, $(p, l_p) = (18, 2)$ in Fig. 1. Via a fine-tuning of the refractive index to $n = n_{\mathrm{opt}} = 2.105\,094\,8$, the modes can be driven into a quasidegeneracy at which their two frequencies

$$x_m = 12.499\,61 - i1.159\,38 \times 10^{-7}, \tag{4}$$

$$x_p = 12.499\,61 - i3.393\,72 \times 10^{-4}, \tag{5}$$

have the same real part but differ in the imaginary parts. Such quasidegeneracies are the starting point to achieve EPs of second order (EP2) in microdisks with extremely weak deformation [19,20].

III. PERTURBATION THEORY FOR QUASIDEGENERATE MODES IN FULLY ASYMMETRIC MICRODISKS

In the following we consider TM polarized fields in a weakly deformed circular cavity whose boundary shape is given in polar coordinates by

$$r(\phi) = R[1 + \lambda f(\phi)], \tag{6}$$

where $f(\phi)$ is the deformation function and λ is a formal perturbation parameter which is set to unity afterwards. In contrast to Refs. [20,32], we here explicitly allow asymmetric deformations $f(\phi) \neq f(-\phi)$. A perturbation theory for a pair of CW and CCW propagating modes without additional quasidegeneracies in such fully asymmetric cavities was discussed in Ref. [36]. In contrast, here we assume two mode pairs (m, l_m) and (p, l_p) with $m \neq p$ whose frequencies have (almost) the same real parts; cf. Fig. 1. Similar to Refs. [20,32], a zeroth-order ansatz for the wave function in the deformed cavity is given by the linear superposition of the modes in a traveling-wave basis as

$$\psi(r, \phi; x) = \sum_{q\in\{\pm m, \pm p\}} a_q\, \psi_q(r, \phi; x), \tag{7}$$

where a_q are the complex amplitudes, and $x = x_m(1 + \delta x)$ is the frequency of the mode in the deformed disk. In the same spirit as Ref. [32] we find that the a_q and δx are determined by the system of equations (see Appendix A)

$$(s_q - \delta x)a_q = \sum_{w\neq q} A_{w-q}\, a_w \tag{8}$$

with $q, w \in \{\pm m, \pm p\}$. The relevant complex Fourier harmonics of the deformation function are

$$A_q = \frac{1}{2\pi R}\int_0^{2\pi} f(\phi)e^{iq\phi}\, d\phi. \tag{9}$$

Furthermore, s_q is given by

$$s_{\pm m} = \frac{S_m(x_m)}{x_m(n^2 - 1)} - A_0, \tag{10}$$

$$s_{\pm p} = \frac{S_p(x_m)}{x_m(n^2 - 1)} - A_0. \tag{11}$$

In order to linearize the system of equations (8) the derivative of S_m is expanded as [32]

$$\frac{\partial S_m}{\partial x}(x) = -(n^2 - 1) - \frac{S_m(x)}{x} - S_m(x)\left[S_m(x) + 2\frac{H_m'}{H_m}(x)\right], \tag{12}$$

with $S_m(x_m) = 0$ and $S_p(x_m) = (n^2 - 1)(x_p - x_m)$. Hence, the frequency x and the amplitudes a_q of the mode in the deformed microdisk are determined by the eigenvalue problem

$$\hat{H}_{\mathrm{TW}} \begin{pmatrix} a_m \\ a_p \\ a_{-p} \\ a_{-m} \end{pmatrix} = x \begin{pmatrix} a_m \\ a_p \\ a_{-p} \\ a_{-m} \end{pmatrix}. \tag{13}$$

Here, $\hat{H}_{\mathrm{TW}}$ is the complex non-Hermitian matrix

$$\hat{H}_{\mathrm{TW}} = \begin{pmatrix} x_m & & & \\ & x_p & & \\ & & x_p & \\ & & & x_m \end{pmatrix} - x_m \times \begin{pmatrix} A_0 & A_{p-m} & A_{-p-m} & A_{-2m} \\ A_{m-p} & A_0 & A_{-2p} & A_{-m-p} \\ A_{m+p} & A_{2p} & A_0 & A_{-m+p} \\ A_{2m} & A_{p+m} & A_{-p+m} & A_0 \end{pmatrix}, \tag{14}$$

which can be regarded as the Hamiltonian in traveling-wave basis (TW). Note that $\hat{H}_{\mathrm{TW}}$ can be transformed in the standing-wave basis (SW) via

$$\hat{H}_{\mathrm{SW}} = B^{-1} \hat{H}_{\mathrm{TW}} \hat{B} \tag{15}$$

with

$$\hat{B} = \frac{1}{\sqrt{2}} \begin{pmatrix} 1 & 0 & 0 & i \\ 0 & 1 & i & 0 \\ 0 & 1 & -i & 0 \\ 1 & 0 & 0 & -i \end{pmatrix}. \tag{16}$$

From Eq. (9) it follows that $A_{-q} = A_q^*$. Thus, $\hat{H}_{\mathrm{TW}}$ divided by x_m has complex conjugate off-diagonal elements which are transformed to real ones in the standing-wave basis as required by reciprocity [37,38]. Note that the diagonal elements of $\hat{H}_{\mathrm{TW}}$ and $\hat{H}_{\mathrm{SW}}$ are complex.

IV. EXCEPTIONAL POINTS OF FOURTH ORDER

In this section we use the perturbation theory to find boundary deformations which exhibit EPs of fourth order. In order to obtain explicit results we specify a set of deformation functions given by

$$\begin{aligned} f(\phi) = d_0 &+ 2\epsilon_1 \cos[(m-p)\phi] + 2\epsilon_2 \sin[(m-p)\phi] \\ &+ 2\delta_1 \cos[(m+p)\phi] + 2\delta_2 \sin[(m+p)\phi] \\ &+ 2\sigma_1 \cos(2m\phi) + 2\sigma_2 \sin(2m\phi) \\ &+ 2\kappa_1 \cos(2p\phi) + 2\kappa_2 \sin(2p\phi), \end{aligned} \tag{17}$$

which allows us to tune the matrix elements of $\hat{H}$ via the nine independent real-valued deformation parameters $\mathcal{S} = (\epsilon_{1/2}, \delta_{1/2}, \sigma_{1/2}, \kappa_{1/2}, d_0)$. However, note that the Hamiltonian $\hat{H}_{\mathrm{TW}}$ in Eq. (14) has additional symmetries with respect to the counterdiagonal such that the existence of an EP4 is *a priori* not guaranteed. Explicitly, $\hat{H}_{\mathrm{TW}}$ with the deformation (17) reads

$$\hat{H}_{\mathrm{TW}} = \begin{pmatrix} x_m & & & \\ & x_p & & \\ & & x_p & \\ & & & x_m \end{pmatrix} - x_m \times \begin{pmatrix} d_0 & \epsilon_1 - i\epsilon_2 & \delta_1 - i\delta_2 & \sigma_1 - i\sigma_2 \\ \epsilon_1 + i\epsilon_2 & d_0 & \kappa_1 - i\kappa_2 & \delta_1 - i\delta_2 \\ \delta_1 + i\delta_2 & \kappa_1 + i\kappa_2 & d_0 & \epsilon_1 - i\epsilon_2 \\ \sigma_1 + i\sigma_2 & \delta_1 + i\delta_2 & \epsilon_1 + i\epsilon_2 & d_0 \end{pmatrix}. \tag{18}$$

TABLE I. The table shows the dimensionless boundary parameters [see Eq. (17)] of EP4s arising from the modes $(m, l_m) = (22, 1)$, $(p, l_p) = (18, 2)$ in a cavity with refractive index $n = 2.105\,094\,8$.

Parameter $\times 10^5$	$\mathcal{S}_1$	$\mathcal{S}_2$
ϵ_1	0.07484865	−0.17533632
ϵ_2	0.04058464	−1.34058502
δ_1	1.34424557	0.02222206
δ_2	−0.14201596	−0.07988964
σ_1	0.03243218	−0.01165198
σ_2	−0.07854319	0.08194345
κ_1	−0.04812878	−0.03233445
κ_2	−0.07003218	0.07619043
d_0	7.14211250	−0.12310027

In order to efficiently search for an EP4 the normalized eigenvectors $\vec{a}^{(i)}$ of $\hat{H}_{\mathrm{TW}}$ with $\sum_q |a_q^{(i)}|^2 = 1$, $i = 1, \ldots, 4$, are obtained numerically. From these eigenvectors a deformation-dependent auxiliary function measuring the nonorthogonality of all four eigenvectors can be defined as

$$g(\mathcal{S}) = \sum_{i \neq j} \left(1 - \left| \sum_q a_q^{(j)*} a_q^{(i)} \right| \right)^2. \tag{19}$$

At an EP4 all four eigenvectors are collinear, i.e., $g = 0$. Since $g \geqslant 0$ holds for all deformations, one can search for minimas of the auxiliary function with $g(\mathcal{S}) \approx 0$ numerically. In the following we present two example systems with an EP4, $\mathcal{S}_1$ and $\mathcal{S}_2$. The corresponding deformation parameters are listed in Table I. In both examples modes with the mode numbers $(m, l_m) = (22, 1)$ and $(p, l_p) = (18, 2)$ (see Fig. 1) coalesce.

At the obtained EP4s there exists only one eigenvalue of the matrix (18) for each system: $x_{\mathrm{EP}} = 12.498\,701 - i1.697\,44 \times 10^{-4}$ for system $\mathcal{S}_1$ and $x_{\mathrm{EP}} = 12.499\,629 - i1.697\,44 \times 10^{-4}$ for system $\mathcal{S}_2$.

The corresponding boundary deformations are shown in Fig. 2. Note that the overall deformation is in both cases of the order $10^{-5}R$, i.e., it is extremely weak. This is self-consistent with the perturbation theory and ensures that the modes are still well-confined whispering-gallery modes in the deformed cavity.

In order to verify that the system is indeed at an EP4, an additional random deformation is applied. Within the perturbation theory this can be realized by selecting a vector $\mathcal{R}$ of nine randomly chosen deformation parameters from the

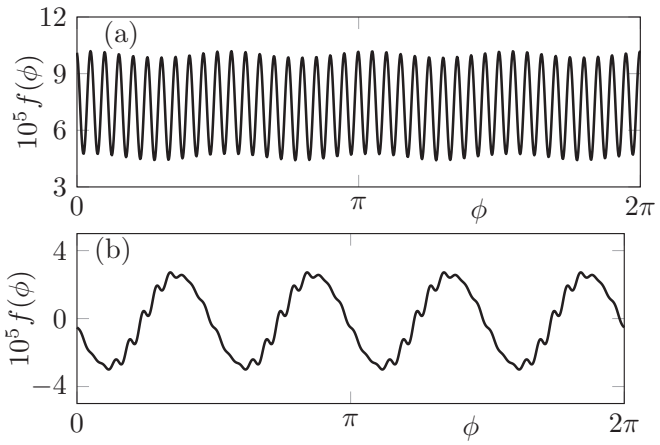

FIG. 2. Dimensionless boundary deformation function $f(\phi)$ [see Eqs. (6) and (17)] for (a) system $\mathcal{S}_1$ and (b) system $\mathcal{S}_2$ (see Table I).

interval $[-1, 1]$. Thus the new deformation is

$$\mathcal{S}_{1/2}(\varepsilon) = \mathcal{S}_{1/2} + \varepsilon\mathcal{R}, \tag{20}$$

where ε sets the strength of the additional deformation that drives the system away from the EP4. In Fig. 3 the frequency dynamics with ε is shown for $\mathcal{S}_1$. For small ε the four complex frequencies approach x_{EP}. The difference $|x - x_{\mathrm{EP}}|$ scales with a quartic root over many magnitudes up to $\varepsilon \approx 10^{-6}$. Such a scaling is expected for an EP4 [1]. If the EP should be utilized for sensing operations, it would require fabrication of the boundary of the cavity with an accuracy according to $\epsilon \prec 10^{-6}$ to benefit from the quartic root scaling. Such an accuracy seems to be beyond today's limitations, which are of the order 10^{-4} [39,40]. However, the presented method to achieve an EP4 is not restricted to such small deformations. With a suitable choice of another initial mode pair one can find an EP4 also for larger deformations as presented in Appendix B.

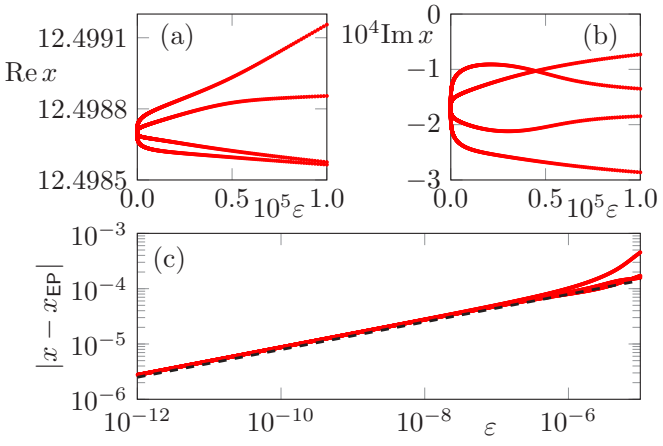

FIG. 3. In (a) and (b) the (red curves) dynamics of the complex frequencies x is shown vs the perturbation strength ε [see Eq. (20)] at the EP4 of $\mathcal{S}_1$. In (c) the corresponding (red curves) differences of the frequencies to x_{EP} are compared to a (black dashed curve) quartic root. All axes are in dimensionless units.

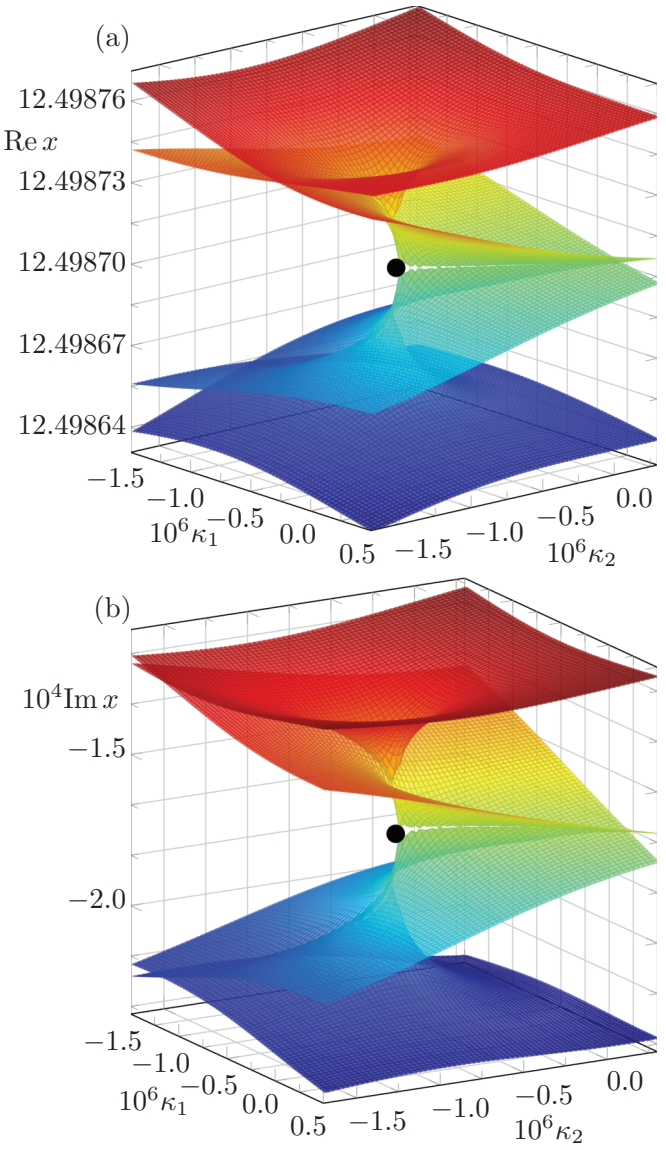

FIG. 4. The (a) real and (b) imaginary parts of the dimensionless complex frequencies x are shown in the κ_1-κ_2 parameter plane around the EP4 of system $\mathcal{S}_1$. A black dot marks EP4. The coloring is according to the value along the z axis from (small) blue to (large) red.

For the EP4 of system $\mathcal{S}_1$ the quartic root topology of the frequencies can also be seen in Fig. 4. Here, the two deformation parameters κ_1 and κ_2 are varied. As a consequence of the root topology, the modes interchange if the system parameters are varied stroboscopically along a closed loop that encloses the EP4 [4,24,41,42]. Hence, a mode needs to be traced along four passes of such a closed loop in parameter space to get back the initial intensity pattern. Note that different behavior occurs if the parameters are varied dynamically in the system [43].

The corresponding mode patterns at the EP4 are shown in Figs. 5(a) and 5(c). From previous works it is known that the mode at an EP2 in a fully asymmetric cavity becomes completely propagating waves in either CW or CCW direction due to asymmetric backscattering [17,18,44]. Here, at the

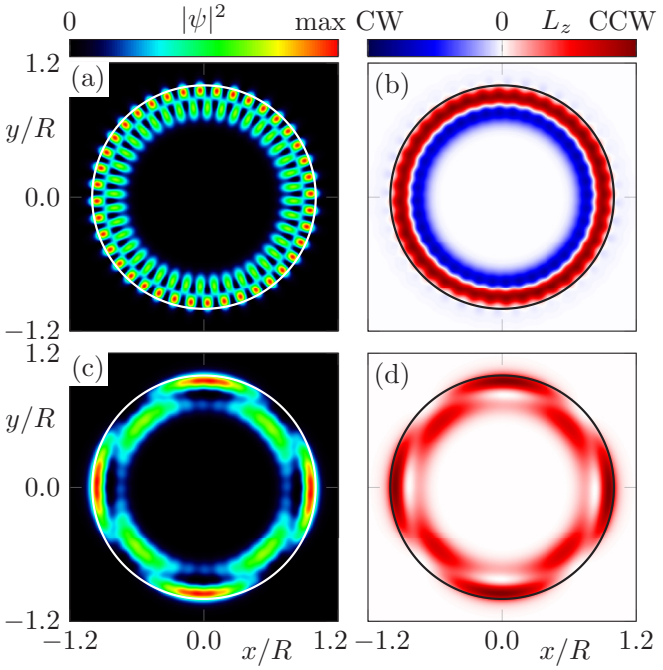

FIG. 5. Mode intensity patterns at EP4 for (a) [(c)] system $\mathcal{S}_1$ [$\mathcal{S}_2$]. In (b) [(d)] the corresponding angular momentum patterns, see Eq. (23), are shown.

EP4 of system $\mathcal{S}_2$ the same phenomenon happens, i.e., there exists one mode with purely CCW propagation and without a CW propagating counterpart. At first glance this is surprising because the Hamiltonian $\hat{H}_{\mathrm{TW}}$ in Eq. (18) has symmetries such that it can be written as

$$\hat{H}_{\mathrm{TW}} = \begin{pmatrix} \Omega & \tilde{K} \\ K & \tilde{\Omega} \end{pmatrix}, \tag{21}$$

with complex 2×2 matrices Ω, $\tilde{\Omega}$, K, and $\tilde{K}$. Thus the off-diagonal blocks describing the conversion of intensity from CW to CCW and vice versa as well as the diagonal blocks have the same (Frobenius-) norm, i.e., $\|K\| = \|\tilde{K}\|$ and $\|\Omega\| = \|\tilde{\Omega}\|$, which is counterintuitive to the two-mode approximation for asymmetric backscattering [15,16,21]. However, it is still possible that the vector $\psi_{\mathrm{EP}} = (\psi_{\mathrm{CCW}}, \psi_{\mathrm{CW}})^{\intercal}$ with $\psi_{\mathrm{CCW}} \neq 0$ and $\psi_{\mathrm{CW}} = 0$ is an eigenvector of $\hat{H}_{\mathrm{TW}}$, namely, if ψ_{CCW} is in the kernel of K, i.e., $K\psi_{\mathrm{CCW}} = 0$, which means that there is effectively no backscattering from CCW to CW propagation for ψ_{EP}.

In contrast, for system $\mathcal{S}_1$ the situation is different. Here, the mode at the EP4 exhibits CW as well as CCW propagating components, and hence it is neither a standing wave nor a wave with a single preferred propagation direction. In order to see this more directly, the current (Poynting vector) can be computed as

$$\vec{j} = (j_x, j_y) \propto \mathrm{Im}\,(\psi^* \vec{\nabla} \psi). \tag{22}$$

The Poynting vector is proportional to the momentum density of the fields. Therefore, at each point in space an angular momentum can be associated to ψ via

$$L_z = x j_y - y j_x, \tag{23}$$

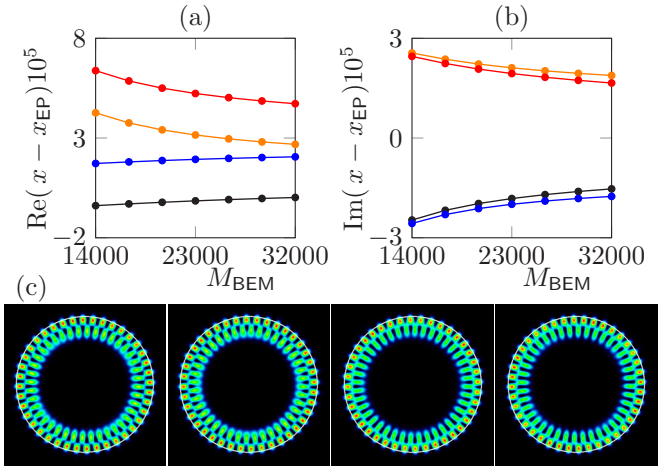

FIG. 6. (a) Real and (b) imaginary part of the difference of numerically computed dimensionless frequencies x and the perturbation theory prediction x_{EP} for system $\mathcal{S}_1$. M_{BEM} is the number of boundary elements. In (c) the intensity mode patterns calculated with BEM are shown.

with $L_z < 0$ ($L_z > 0$) indicating CW (CCW) propagation. For both systems $\mathcal{S}_{1/2}$ the angular momentum patterns of the modes are shown in Figs. 5(b) and 5(d). The mode of system $\mathcal{S}_1$ exhibits two ringlike structures. Close to the cavity's boundary the mode propagates in CCW direction whereas in the inner shell it is propagating clockwise. Such global counterpropagating behavior has so far not been observed in deformed microdisk cavities. In Ref. [20], however, local vortex structures with different propagation directions have been observed at EPs of third order in cavities with a mirror reflection symmetry.

In order to test the results from the perturbation theory, we also performed full numerical simulations using the boundary element method (BEM) [45]. The perturbation theory provides approximations for solutions of the mode equation (1) and on the other hand, full numerical simulations have small errors du to finite discretizations, e.g., of the cavity's boundary. Thus, the deformation predicted for the EP4 is not exactly the one where full numerical simulations would show an EP4. Therefore, with the BEM we can calculate four modes very close in the complex plane. As shown in Fig. 6 for system $\mathcal{S}_1$, depending on the number of boundary elements the numerical results for the complex frequencies slowly converge, with an overall difference of the order 10^{-5}, to the predictions from the perturbation theory. As can be seen in Fig. 6(c), the corresponding numerically calculated mode patterns are all similar and in good agreement to the prediction from perturbation theory [see Fig. 5(a)]. This is quantified by the pairwise overlap

$$S[\psi_1, \psi_2] = \frac{\left| \int_{\mathrm{cavity}} \psi_1^* \psi_2 \, d^2 r \right|}{\sqrt{\int_{\mathrm{cavity}} |\psi_1|^2 \, d^2 r \int_{\mathrm{cavity}} |\psi_2|^2 \, d^2 r}}, \tag{24}$$

which is larger than 0.95 for the modes $\psi_{\mathrm{BEM,\,i}}$ calculated with BEM in Fig. 6(c). Additionally, the modes show the characteristic self-orthogonality [29,46] at the EP with $S[\psi^*_{\mathrm{BEM,\,i}}, \psi_{\mathrm{BEM,\,i}}] < 0.05$ for $i = 1, .., 4$. This confirms that

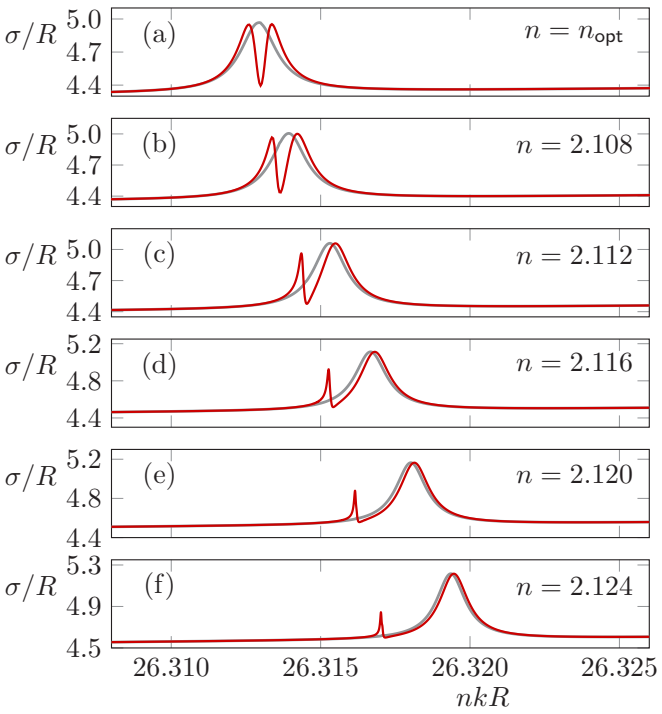

FIG. 7. Cross section for plane waves with dimensionless wave number $kR \in \mathbb{R}$ of (red curves) system $\mathcal{S}_2$ and (light gray curves) a circular cavity for different refractive indexes.

the deformation predicted by the perturbation theory is indeed very close to an EP4. Note that an example where the perturbation theory is applied to a generic deformation without an EP is discussed in Appendix C.

V. PLANE-WAVE SCATTERING

A method to measure optical modes is the scattering cross section $\sigma(\vec{k})$ with incident plane waves given by a real-valued wave vector $\vec{k} = k(1, 0)$. As described in Ref. [45], the cross section can be calculated with the BEM from the differential scattering amplitude $f(\theta, \vec{k})$ using the optical theorem

$$\sigma(k) = 2\sqrt{\frac{\pi}{k}}\,\mathrm{Im}\,[(1-i)f(\theta=\phi,\vec{k})]. \tag{25}$$

It is known that the cross section can have a Fano-type profile if the system is at an EP [47–49]. This is shown for the system $\mathcal{S}_2$ (at the EP4) in Fig. 7(a). By slightly increasing the refractive index of the cavity, the non-Hermitian degeneracy is lifted such that individual modes arise from the EP4. As shown in Figs. 7(a)–7(f) the refractive index change has two effects on the cross section: (i) the resonant frequencies show an overall shift with increasing n and (ii) the Fano-type profile is split into a very narrow peak for two modes with a high Q factor and a relatively broad peak for two modes with a lower Q factor. As an example, the Q factor of the modes corresponding to the broad (narrow) peak in a microdisk with refractive index $n = 2.124$ [cf. Fig. 7(f)] are around 23 500 (1 130 000). Note that an overall frequency shift is also observable in the circular cavity, whereas the splitting into distinct peaks of the cross section for such small refractive index changes can only be observed in the deformed cavity at the EP.

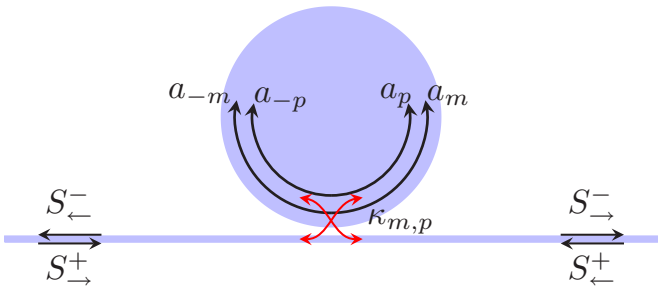

FIG. 8. Illustration of a microdisk cavity coupled to a waveguide.

VI. TRANSMISSION AND REFLECTION SPECTRA VIA AN ATTACHED WAVEGUIDE

In contrast to the free plane-wave scattering in experiment, often a waveguide is placed next to the cavity to measure the transmission or reflection spectra as illustrated in Fig. 8. However, such a waveguide also disturbs the cavity modes such that the spectra measured via the waveguide and the one from plane waves are not identical. In this section we combine the perturbation theory from Sec. III with the coupled-mode theory [50–52] that describes the interaction of the cavity with an attached waveguide. This allows us to predict the reflection and transmission spectra of the deformed microdisk measured via a waveguide.

A. Coupled-mode theory

In coupled-mode theory the time-dependent amplitudes $\vec{a} = (a_m, a_p, a_{-p}, a_{-m})^\intercal$ of the propagating waves with the relevant angular momentum $(m, p, -p, -m)$ in the microcavity are described by a Schrödinger-type equation

$$i\frac{d}{dt}\vec{a}(t) = \hat{H}_{\mathrm{TW}}\vec{a}(t) + i\vec{P}(t), \tag{26}$$

where $\vec{P}$ is an effective pump term from the power input to the cavity via the waveguide modes. It can be written as

$$\vec{P}(t) = \vec{\kappa}_{\mathrm{CCW}}S^+_{\rightarrow}(t) + \vec{\kappa}_{\mathrm{CW}}S^+_{\leftarrow}(t). \tag{27}$$

Here, $S^+_{\rightarrow}$ ($S^+_{\leftarrow}$) are the amplitudes of the waveguide modes, and $\vec{\kappa}_{\mathrm{CCW}}$ ($\vec{\kappa}_{\mathrm{CW}}$) are vectors with coefficients describing the coupling from the waveguide and the propagating waves inside the cavity if the system is excited from the left (right). The coupling coefficients depend on the specific system setup, e.g., the distance of the waveguide to the cavity or the deformation of the cavity close to the waveguide. For simplicity we assume that the coupling is determined by only two coupling coefficients $\kappa_{m,p}$ such that $\vec{\kappa}_{\mathrm{CCW}} = (\kappa_m, \kappa_p, 0, 0)^\intercal$ and $\vec{\kappa}_{\mathrm{CW}} = (0, 0, \kappa_p, \kappa_m)^\intercal$. This means from the left waveguide port excites only CCW propagating waves whereas via an excitation from the right waveguide port only CW propagating waves inside the cavity are excited. This can be achieved by placing the waveguide sufficiently away from the cavity, backscattering due to the cavity-waveguide coupling being neglected.

If the (dimensionless) excitation frequency is $\omega_e \in \mathbb{R}$, the amplitudes of the fields in the waveguide can be written as $S^{\pm}_{\leftrightarrows}(t) = s^{\pm}_{\leftrightarrows} e^{-i\omega_e t}$ with constants $s^{\pm}_{\leftrightarrows}$. Thus inside the cavity the amplitudes are given by $\vec{a}(t) = \vec{c}e^{-i\omega_e t}$ with constants $\vec{c}$. Inserting this ansatz into Eq. (26) yields

$$i(\hat{H}_{\mathrm{TW}} - \omega_e \hat{\mathbf{1}})\vec{c} = \vec{P}_0 \tag{28}$$

with $\vec{P}_0 = (\kappa_m s^+_{\rightarrow}, \kappa_p s^+_{\rightarrow}, \kappa_p s^+_{\leftarrow}, \kappa_m s^+_{\leftarrow})^{\intercal}$. A formal solution of this equation is given in terms of the Green's function $\hat{G}(\omega_e) = (\omega_e \hat{\mathbf{1}} - \hat{H}_{\mathrm{TW}})^{-1}$ as

$$\vec{c} = i\hat{G}(\omega_e)\vec{P}_0 + \vec{c}_H, \tag{29}$$

where $\vec{c}_H$ is the solution of the homogeneous system with vanishing $\vec{P}_0$. Since we assume the excitation via the waveguide only we can neglect the term $\vec{c}_H$ here. An advantage of the perturbation theory is that it directly provides the Hamiltonian $\hat{H}_{\mathrm{TW}}$ via Eq. (14). Therefore also the Green's function $\hat{G}(\omega_e)$ is directly accessible. In the particular case of an EP4 Green's function it can be written explicitly as [53]

$$\hat{G}(\omega_e) = \frac{\hat{\mathbf{1}}}{\omega_e - x_{\mathrm{EP}}} + \frac{\hat{M}_1}{(\omega_e - x_{\mathrm{EP}})^2} + \frac{\hat{M}_2}{(\omega_e - x_{\mathrm{EP}})^3} + \frac{\hat{M}_3}{(\omega_e - x_{\mathrm{EP}})^4}, \tag{30}$$

with $\hat{M}_k = (\hat{H}_{\mathrm{TW}} - x_{\mathrm{EP}}\hat{\mathbf{1}})^k$. Here, the terms involving $\hat{M}_k$ with $k \geqslant 1$ can lead to a non-Lorentzian behavior in the spectra [48,54]. However, note that in the following it is sufficient to evaluate $(\omega_e \hat{\mathbf{1}} - \hat{H}_{\mathrm{TW}})^{-1}$ numerically.

In order to obtain the transmission and reflection spectra, the outgoing waveguide amplitudes $s^-_{\leftrightarrows}$ need to be calculated. In the coupled-mode theory these coefficients are given by

$$s^-_{\leftarrow} = s^+_{\leftarrow} - \vec{\kappa}^{\dagger}_{\mathrm{CW}}\vec{c}, \tag{31a}$$

$$s^-_{\rightarrow} = s^+_{\rightarrow} - \vec{\kappa}^{\dagger}_{\mathrm{CCW}}\vec{c}. \tag{31b}$$

Putting in the solution (29) for $\vec{c}$ we can calculate the transmission coefficient $t_L(t_R)$ for excitation from the left (right) as well as the corresponding reflection coefficients $r_L(r_R)$ as

$$t_{\mathrm{L}} = \left.\frac{s^-_{\rightarrow}}{s^+_{\rightarrow}}\right|_{s^+_{\leftarrow}=0} = 1 - i\vec{\kappa}^{\dagger}_{\mathrm{CCW}}\hat{G}(\omega_e)\vec{\kappa}_{\mathrm{CCW}}, \tag{32a}$$

$$r_{\mathrm{L}} = \left.\frac{s^-_{\leftarrow}}{s^+_{\rightarrow}}\right|_{s^+_{\leftarrow}=0} = -i\vec{\kappa}^{\dagger}_{\mathrm{CW}}\hat{G}(\omega_e)\vec{\kappa}_{\mathrm{CCW}}, \tag{32b}$$

$$t_{\mathrm{R}} = \left.\frac{s^-_{\leftarrow}}{s^+_{\leftarrow}}\right|_{s^+_{\rightarrow}=0} = 1 - i\vec{\kappa}^{\dagger}_{\mathrm{CW}}\hat{G}(\omega_e)\vec{\kappa}_{\mathrm{CW}}, \tag{32c}$$

$$r_{\mathrm{R}} = \left.\frac{s^-_{\rightarrow}}{s^+_{\leftarrow}}\right|_{s^+_{\rightarrow}=0} = -i\vec{\kappa}^{\dagger}_{\mathrm{CCW}}\hat{G}(\omega_e)\vec{\kappa}_{\mathrm{CW}}. \tag{32d}$$

Note that reciprocity requires $t_{\mathrm{L}} = t_{\mathrm{R}}$, which is fulfilled due to the choice of $\vec{\kappa}_{\mathrm{CW}}$ and $\vec{\kappa}_{\mathrm{CCW}}$. The strategy to obtain explicit results is the following. First, we simulate numerically a circular cavity and an attached a waveguide with a certain width and distance to the cavity. From these simulations we deduce the coupling parameter $\kappa_{m/p}$ and the frequency shifts of the modes in the circular cavity due to the presence of the waveguide. Afterwards we can apply Eqs. (32) to get results for arbitrary weakly deformed microdisks.

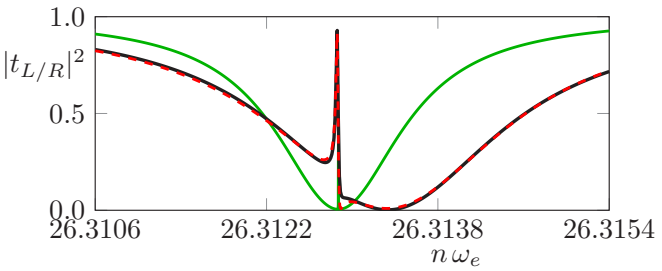

FIG. 9. Transmission spectrum of a circular cavity coupled to a waveguide. The fully numerically computed spectrum is shown as a black curve. The red dashed curve is the result of Eq. (33) with the fitted parameters (35). The light green curve is the result of Eq. (33) for unshifted frequencies $x_{m/p}$ and $(\kappa_m, \kappa_p) = (0.000\,37, 0.019)$.

B. Circular microdisk coupled to a waveguide

For the special case of a circular disk with no deformation the Hamiltonian $\hat{H}_{\mathrm{TW}}$ is diagonal as can be seen from Eq. (14) such that the reflection and transmission coefficients from Eqs. (32a)–(32d) can be simplified to

$$t_{L/R} = 1 - i\left(\frac{|\kappa_m|^2}{\omega_e - \tilde{x}_m} + \frac{|\kappa_p|^2}{\omega_e - \tilde{x}_p}\right), \tag{33}$$

$$r_{L/R} = 0. \tag{34}$$

However, due to the interaction of the attached waveguide with the circular cavity the complex frequencies of the modes $\tilde{x}_{m/p}$ are not exactly the ones from the bare circular cavity $x_{m/p}$ [see Eqs. (4) and (5)] computed as roots of Eq. (2). In order to get $\tilde{x}_{m/p}$ as well as the coupling parameters $\kappa_{m/p}$ we simulate the transmission spectrum of the circular cavity attached to a waveguide using COMSOL MULTIPHYSICS 5.4 and apply a fit of $|t_{L/R}|^2$ using Eq. (33), see Fig. 9. In the example a waveguide of width $0.03R$ is placed $0.32R$ away from the cavity. A very good agreement of Eq. (33) with the simulation is obtained for

$$\kappa_m \approx 2.370\,691 \times 10^{-3}, \tag{35a}$$

$$\kappa_p \approx 2.356\,105 \times 10^{-2}, \tag{35b}$$

$$\tilde{x}_m \approx 12.499\,610 - i5.353\,616 \times 10^{-6}, \tag{35c}$$

$$\tilde{x}_p \approx 12.499\,842 - i6.153\,160 \times 10^{-4}. \tag{35d}$$

Note that the slight shift of the complex frequencies due to the waveguide is crucial since adjusting $\kappa_{m/p}$ only (see green curve in Fig. 9) is not sufficient to reproduce the simulated transmission spectra.

C. Weakly deformed microdisks coupled to a waveguide

With the computed waveguide coupling coefficients of the circular cavity we can now apply Eqs. (32) to predict the transmission and the reflection spectra of a deformed microdisk. For system $\mathcal{S}_1$ ($\mathcal{S}_2$) the results are shown in Fig. 10 (Fig. 11). For both systems in general a very good agreement to full numerical simulations is obtained for the transmission as well as the reflection spectra. The transmission spectra in both

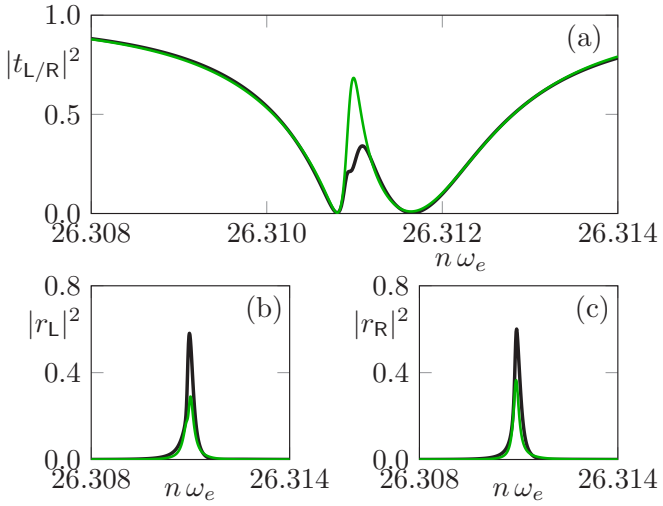

FIG. 10. (a) Transmission spectrum and (b)/(c) reflection spectra for excitation from left/right of the cavity $\mathcal{S}_1$ coupled to a waveguide. The fully numerically computed spectra is shown as a black curve. The light green curve is the result of Eqs. (32) with the coupling parameters (35).

cases show a Fano-type profile which is slightly asymmetric in comparison to the cross section for plane waves. In system $\mathcal{S}_1$ the peak in the transmission is slightly less pronounced, as predicted by the perturbation theory. However, the shift of the overall spectrum in $n\omega_e$ via the deformation is in both cases predicted accurately by Eqs. (32). What is remarkable is the asymmetric backscattering [15,16,18] in system $\mathcal{S}_2$. Here, the reflection coefficient for excitation from the left almost vanishes, whereas it is finite for excitation from the right. This is in good agreement with the fact that the mode of system $\mathcal{S}_2$ at the EP4 is a pure CCW propagating wave, see Figs. 5(c) and 5(d). For both systems the reflection coefficient tends to be

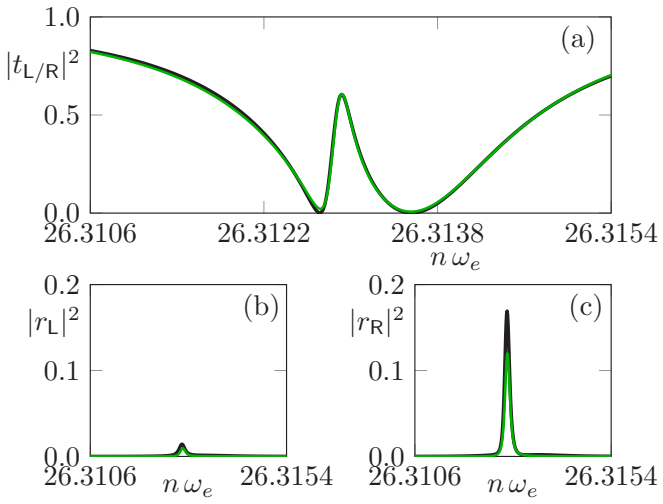

FIG. 11. (a) Transmission spectrum and (b)/(c) reflection spectra for excitation from left/right of the cavity $\mathcal{S}_2$ coupled to a waveguide. The fully numerically computed spectra is shown as black curve. The light green curve is the result of Eqs. (32) with the coupling parameters (35).

slightly underestimated, which might be due to an enhanced cavity-waveguide coupling due to the deformation [55].

VII. SUMMARY

In this paper we have extended the perturbation theory for quasidegenerate modes in weakly deformed cavities to fully asymmetric deformations. This allows us to tune the deformation such that four modes, i.e., the clockwise and counterclockwise components for two different mode numbers, coalesce into one single mode. Such deformations mark an exceptional point of fourth order in parameter space. Explicitly we discussed two example deformations where the modes at the exceptional points have interesting properties: In the one example the mode exhibits regions of pure clockwise as well as pure counterclockwise propagation, whereas in the other example the mode is a purely counterclockwise propagating wave. Such more complicated propagating wave patterns might find applications for orbital-angular-momentum lasers. Additionally, we discussed the cross section of plane-wave scattering and measurements of transmission and reflection spectra via a waveguide attached to the cavity. For the later we used coupled-mode theory in combination with the perturbation theory to describe the observed behavior of the transmission and reflection coefficient.

Our approach is so far restricted to TM polarized fields. A generalization to TE polarization is a challenging future task due to the more complicated boundary conditions. In the TE case already the perturbation theory for well-separated modes in a microcavity with mirror-reflection symmetry is much more difficult [56] and reveals pitfalls [57]. Moreover, a proper treatment of quasidegenerate modes in asymmetrically deformed cavities is not known so far for TE polarized fields.

ACKNOWLEDGMENTS

The authors would like to thank M. Khanbekyan for helpful discussions. This work was supported by the DFG (Project No. WI1986/7-1).

APPENDIX A: DERIVATION OF THE PERTURBATION THEORY

In this Appendix we comment on the derivation of the perturbation theory for quasidegenerate modes of the circular cavity. At such a quasidegeneracy with $\mathrm{Re}\,x_m = \mathrm{Re}\,x_p$ the expansion coefficients a_q in Eq. (7) with $q \in \{\pm m, \pm p\}$ are of zeroth order in the perturbation parameter λ. Therefore, even for extremely weak deformations it is important to chose the correct linear combination of the unperturbed modes. In order to construct this linear combination and the frequency x in the deformed cavity the boundary conditions at the dielectric interface are evaluated in a series of the perturbation parameter λ (see Ref. [32] for more details). The first order of the boundary condition for the normal derivative $\partial_{\bar{\nu}}\psi_1 = \partial_{\bar{\nu}}\psi_2$ results in the equation

$$\partial_r[\psi_1 - \psi_2]\big|_{(R,\phi)} = -\lambda f(\phi)\,\partial_r^2[\psi_1 - \psi_2]\big|_{(R,\phi)}. \tag{A1}$$

With the ansatz (7) the derivatives can be calculated as

$$\partial_r[\psi_1 - \psi_2]|_{(R,\phi)} = k \sum_p a_p S_p(x)\chi_p(\phi) \tag{A2}$$

$$\partial_r^2[\psi_1 - \psi_2]|_{(R,\phi)} = -\frac{k}{R}\sum_p a_p[x(n^2-1) + S_p(x)]\chi_p(\phi). \tag{A3}$$

Inserting these derivatives in Eq. (A1), introducing A_{p-q} via Eq. (9), and using the orthogonality of $\chi_p(\phi) = e^{ip\phi}$ yields

$$S_q(x)a_q = \lambda \sum_p A_{p-q}[x(n^2-1) + S_p(x)]a_p. \tag{A4}$$

Because of the prefactor λ the terms in the sum need to be evaluated for $x = x_0$. Therefore, we can neglect the term $S_p(x_0)$ in the sum as from the continuity of the wave function along the cavity's interface following

$$0 = [\psi_1 - \psi_2]|_{(r(\phi),\phi)} \tag{A5}$$

$$= \underbrace{[\psi_1 - \psi_2]|_{(R,\phi)}}_{=0} + \lambda f(\phi) \underbrace{\partial_r[\psi_1 - \psi_2]|_{(R,\phi)}}_{\sim \sum_p a_p S_p(x_0)}. \tag{A6}$$

Thus, by setting λ formally to 1 and expanding to $x = x_0(1 + \delta x)$ we get

$$S_q[x_0(1+\delta x)]a_q = \sum_p x_0(n^2-1)A_{p-q}a_p, \tag{A7}$$

which is the equivalent equation to Refs. [20,32]. Next, we explicitly use the series expansion of S_q around x_0 as

$$S_q[x_0(1+\delta x)] \approx S_q(x_0) + x_0\delta x \frac{\partial S_q}{\partial x}(x_0), \tag{A8}$$

with the leading order of the derivative from Eq. (12), i.e., $\partial S_q/\partial x = -(n^2-1)$. Therefore, it yields

$$[S_q(x_0) - x_0\delta x(n^2-1)]a_q = \sum_p (n^2-1)x_0 A_{p-q}a_p\,, \tag{A9}$$

which is equivalent to Eq. (8) for $x_0 = x_m$.

APPENDIX B: EXAMPLE FOR AN EXCEPTIONAL POINT WITH A LARGER BOUNDARY DEFORMATION

In this Appendix we present another example where an EP of fourth order can be achieved with a larger deformation via a suitable choice of the initial modes in the circular cavity. Here, we choose the modes $(m, l_m) = (14, 2)$ and $(p, l_p) = (11, 3)$, which have a quasidegeneracy for the refractive index $n = 2.602\,536\,8$ with $x_m = 8.376\,42 - i4.887\,00 \times 10^{-5}$, $x_p = 8.376\,42 - i8.299\,17 \times 10^{-3}$. Hence, in the complex frequency plane these modes are more separated than the modes from Eqs. (4) and (5). Applying the optimization for the deformation parameters reveals an EP of fourth order for $(d_0, \epsilon_1, \epsilon_2, \delta_1, \delta_2, \sigma_1, \sigma_2, \kappa_1, \kappa_2) \approx 10^{-4}$ $(0.031\,95, 0.010\,12, 0.978\,26, 0.069\,57, -4.729\,86, 0.004\,18, -0.958\,80, -0.024\,02, 0.958\,51)$ with $x_{\mathrm{EP}} \approx 8.3764 - i0.0042$. These deformation parameters are about a magnitude larger than the ones from Table I. The corresponding intensity and angular momentum patterns of the mode at EP4 are shown in Fig. 12.

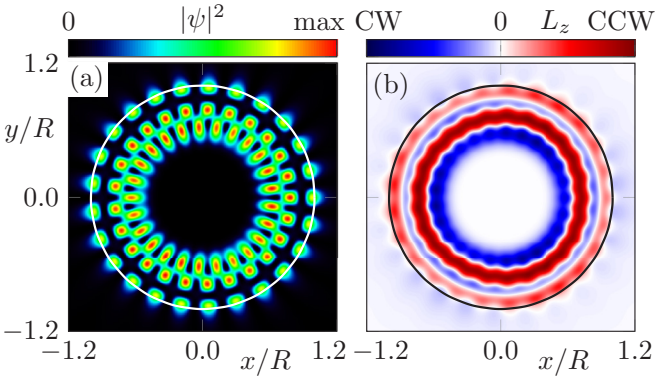

FIG. 12. Mode (a) intensity and (b) angular momentum patterns of the mode at the EP4 described in Appendix B.

APPENDIX C: DEFORMATIONS WITHOUT EXCEPTIONAL POINTS

The presented perturbation theory for quasidegenerate modes in a weakly deformed fully asymmetric cavity is not restricted to deformations of the form (17). It can be applied also to generic deformations by calculating the matrix elements of the Hamiltonian (14) via Eq. (9). In this Appendix we present results and limitations of this approach for a circular cavity with two asymmetric notches. The boundary of the cavity is defined in polar coordinates by

$$\frac{r(\phi)}{R} = 1 - \sum_{\nu,l} \epsilon_\nu \exp\left[-(\phi - \phi_\nu + 2\pi l)^2/\left(2\sigma_\nu^2\right)\right], \tag{C1}$$

where ϵ_ν, σ_ν, and ϕ_ν are parameters for the depth, width, and angular position of the notch $\nu \in \{1, 2\}$. The sum over $l \in \mathbb{Z}$ ensures $r(\phi)$ to be a 2π-periodic function. In the following the parameters $(\epsilon_1, \sigma_1, \epsilon_2, \sigma_2, \phi_2) = (0.02, 0.04, 0.015, 0.02, 0)$ are fixed and $\phi_1 \in [0.3\pi, 0.4\pi]$ is varied. We consider the quasidegenerate modes $(m, l_m) = (22, 1)$ and $(p, l_p) =$

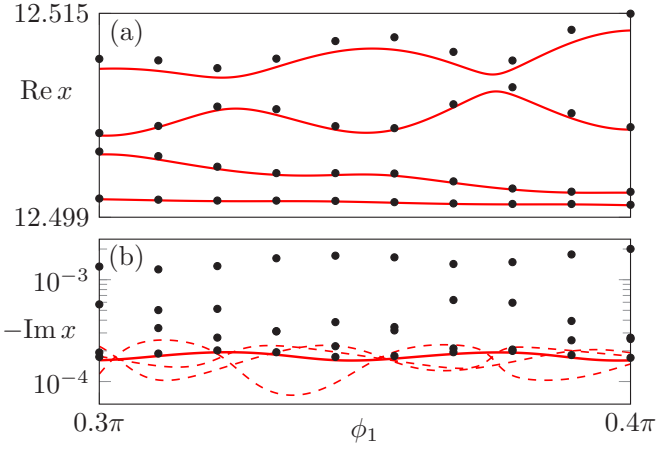

FIG. 13. The (a) real and (b) imaginary part of the mode's frequencies in an asymmetric cavity with two notches [see Eq. (C1)]. The angular position ϕ_1 of one notch is varied. Numerically computed values from BEM are shown as dots. Reliable (inaccurate) predictions from the perturbation theory are represented by solid (dashed) curves.

(12, 2) [see Eqs. (4) and (5)] in a cavity with refractive index $n = 2.105\,094\,8$. As shown in Fig. 13 the results from the perturbation theory for the real part of the frequencies are in very good agreement to full numerical simulations with BEM results. However, the perturbation theory cannot describe the change in the imaginary part of the frequencies for all the modes. Only for the mode with the lowest losses a prediction of the imaginary part of the frequency fits [see solid curve in Fig. 13(b)]. Note that it is already known from Refs. [32,36,58] that the first-order corrections in the perturbation theory are not sufficient to predict the imaginary part of the frequencies well. In the same spirit the Hamiltonian (14) cannot describe loss channels arising from a coupling between modes other than (m, l_m), (p, l_p). However, these loss channels become important for arbitrary deformations, whereas they are suppressed for boundaries of the form (17).

[1] T. Kato, *Perturbation Theory for Linear Operators* (Springer, New York, 1966).
[2] W. D. Heiss, Phys. Rev. E **61**, 929 (2000).
[3] M. V. Berry, Czech. J. Phys. **54**, 1039 (2004).
[4] C. Dembowski, H.-D. Gräf, H. L. Harney, A. Heine, W. D. Heiss, H. Rehfeld, and A. Richter, Phys. Rev. Lett. **86**, 787 (2001).
[5] C. Dembowski, B. Dietz, H.-D. Gräf, H. L. Harney, A. Heine, W. D. Heiss, and A. Richter, Phys. Rev. E **69**, 056216 (2004).
[6] S.-B. Lee, J. Yang, S. Moon, S.-Y. Lee, J.-B. Shim, S. W. Kim, J.-H. Lee, and K. An, Phys. Rev. Lett. **103**, 134101 (2009).
[7] J. Zhu, Ş. K. Özdemir, L. He, and L. Yang, Opt. Express **18**, 23535 (2010).
[8] B. Peng, Ş. K. Özdemir, F. Lei, F. Monfi, M. Gianfreda, G. L. Long, S. Fan, F. Nori, C. M. Bender, and L. Yang, Nat. Phys. **10**, 394 (2014).
[9] Y. Shin, H. Kwak, S. Moon, S.-B. Lee, J. Yang, and K. An, Sci. Rep. **6**, 38826 (2016).
[10] A. Regensburger, C. Bersch, M.-A. Miri, G. Onishchukov, D. N. Christodoulides, and U. Peschel, Nature (London) **488**, 167 (2012).
[11] Y. Choi, S. Kang, S. Lim, W. Kim, J.-R. Kim, J.-H. Lee, and K. An, Phys. Rev. Lett. **104**, 153601 (2010).
[12] M. Brandstetter, M. Liertzer, C. Deutsch, P. Klang, J. Schöberl, H. E. Türeci, G. Strasser, K. Unterrainer, and S. Rotter, Nat. Commun. **5**, 4034 (2014).
[13] T. Gao, E. Estrecho, K. Y. Bliokh, T. C. H. Liev, M. D. Fraser, S. Brodbeck, M. Kamp, C. Schneider, S. Höfling, Y. Yamamoto, F. Nori, Y. S. Kivshar, A. G. Truscott, R. G. Dall, and E. A. Ostrovskaya, Nature (London) **526**, 554 (2015).
[14] H. Cao and J. Wiersig, Rev. Mod. Phys. **87**, 61 (2015).
[15] J. Wiersig, S. W. Kim, and M. Hentschel, Phys. Rev. A **78**, 053809 (2008).
[16] J. Wiersig, A. Eberspächer, J.-B. Shim, J.-W. Ryu, S. Shinohara, M. Hentschel, and H. Schomerus, Phys. Rev. A **84**, 023845 (2011).
[17] J. Wiersig, Phys. Rev. A **84**, 063828 (2011).
[18] B. Peng, Ş. K. Özdemir, M. Liertzer, W. Chen, J. Kramer, H. Yılmaz, J. Wiersig, S. Rotter, and L. Yang, Proc. Nat. Acad. Sci. USA, **113**, 6845 (2016).
[19] C.-H. Yi, J. Kullig, and J. Wiersig, Phys. Rev. Lett. **120**, 093902 (2018).
[20] J. Kullig, C.-H. Yi, and J. Wiersig, Phys. Rev. A **98**, 023851 (2018).
[21] J. Wiersig, Phys. Rev. A **89**, 012119 (2014).
[22] J. Wiersig, Phys. Rev. A **93**, 033809 (2016).
[23] W. Chen, Ş. K. Özdemir, G. Zhao, J. Wiersig, and L. Yang, Nature (London) **548**, 192 (2017).
[24] G. Demange and E.-M. Graefe, J. Phys. A: Math. Theor. **45**, 025303 (2012).
[25] M. H. Teimourpour, R. El-Ganainy, A. Eisfeld, A. Szameit, and D. N. Christodoulides, Phys. Rev. A **90**, 053817 (2014).
[26] Q. Zhong, D. N. Christodoulides, M. Khajavikhan, K. G. Makris, and R. El-Ganainy, Phys. Rev. A **97**, 020105(R) (2018).
[27] K. Ding, G. Ma, M. Xiao, Z. Q. Zhang, and C. T. Chan, Phys. Rev. X **6**, 021007 (2016).
[28] H. Jing, Ş. K. Özdemir, H. Lü, and F. Nori, Sci. Rep. **7**, 3386 (2017).
[29] W. D. Heiss, J. Phys. A: Math. Theor. **41**, 244010 (2008).
[30] H. Hodaei, A. Hassan, S. Wittek, H. Carcia-Cracia, R. El-Ganainy, D. Christodoulides, and M. Khajavikhan, Nature (London) **548**, 187 (2017).
[31] J. D. Jackson, *Classical Electrodynamics* (John Wiley and Sons, New York, 1962).
[32] R. Dubertrand, E. Bogomolny, N. Djellali, M. Lebental, and C. Schmit, Phys. Rev. A **77**, 013804 (2008).
[33] C. P. Dettmann, G. V. Morozov, M. Sieber, and H. Waalkens, Europhys. Lett. **87**, 34003 (2009).
[34] E. Bogomolny, R. Dubertrand, and C. Schmit, Phys. Rev. E **78**, 056202 (2008).
[35] C.-H. Yi, J. Kullig, M. Hentschel, and J. Wiersig, Photonics Res. **7**, 464 (2019).
[36] J. Kullig and J. Wiersig, Phys. Rev. A **94**, 043850 (2016).
[37] M. M. Sternheim and J. F. Walker, Phys. Rev. C **6**, 114 (1972).
[38] H.-J. Stöckmann, E. Persson, Y.-H. Kim, M. Barth, U. Kuhl, and I. Rotter, Phys. Rev. E **65**, 066211 (2002).
[39] D. Parrain, C. Baker, G. Wang, B. Guha, E. G. Santos, A. Lemaitre, P. Senellart, G. Leo, S. Ducci, and I. Favero, Opt. Express **23**, 19656 (2015).
[40] A. Cerjan, S. Bittner, M. Constantin, M. Guy, Y. Zeng, Q. Jie Wang, H. Cao, and A. Stone, arXiv:1908.05397.
[41] W. D. Heiss, J. Phys. A: Math. Theor. **45**, 444016 (2012).
[42] M. Müller and I. Rotter, J. Phy. A: Math. Theor. **41**, 244018 (2008).
[43] J. Doppler, A. A. Mailybaev, J. Böhm, U. Kuhl, A. Girschik, F. Libisch, T. J. Milburn, P. Rabl, N. Moiseyev, and S. Rotter, Nature (London) **537**, 76 (2016).
[44] J. Wiersig, Non-Hermitian effects due to asymmetric backscattering of light in whispering-gallery microcavities, in *Parity-time Symmetry and Its Applications*, edited by D. Christodoulides and J. Yang (Springer Singapore, Singapore, 2018), pp. 155–184.
[45] J. Wiersig, J. Opt. A: Pure Appl. Opt. **5**, 53 (2003).
[46] N. Moiseyev, *Non-Hermitian Quantum Mechanics* (Cambridge University Press, Cambridge, England, 2011).

[47] L. Schwarz, H. Cartarius, G. Wunner, W. D. Heiss, and J. Main, Eur. Phys J. D **69**, 196 (2015).
[48] W. D. Heiss and G. Wunner, Eur. Phys. J D **68**, 284 (2014).
[49] A. I. Magunov, I. Rotter, and S. I. Strakhova, Phys. Rev. B **68**, 245305 (2003).
[50] T. J. Kippenberg, S. M. Spillane, and K. J. Vahala, Opt. Lett. **27**, 1669 (2002).
[51] C. Manolatou, M. J. Khan, S. Fan, P. R. Villeneuve, H. A. Haus, and J. D. Joannopoulos, IEEE J. Quant. Electron. **35**, 1322 (1999).
[52] J.-B. Shim, P. Schlagheck, M. Hentschel, and J. Wiersig, Phys. Rev. A **94**, 053849 (2016).
[53] W. D. Heiss, Int. J. Theor. Phys. **54**, 3954 (2015).
[54] M. Khanbekyan (private communication, 2019).
[55] X. Jiang, L. Shao, S.-X. Zhang, X. Yi, J. Wiersig, L. Wang, Q. Gong, M. Lončar, L. Yang, and Y.-F. Xiao, Science **358**, 344 (2017).
[56] L. Ge, Q. H. Song, B. Redding, and H. Cao, Phys. Rev. A **87**, 023833 (2013).
[57] M. Badel and J. Wiersig, Phys. Rev. A **99**, 063825 (2019).
[58] J. Wiersig, Phys. Rev. A **85**, 063838 (2012).